Laminar conjugate natural convection in horizontal annuli

N.B. Sambamurthy, A. Shaija, G.S.V.L. Narasimham *, M.V. Krishna Murthy [1]

Department of Mechanical Engineering, Indian Institute of Science, Bangalore 560 012, India

ARTICLE INFO

ABSTRACT

A numerical study of two-dimensional conjugate natural convection in a horizontal cylindrical annulus formed between an inner heat generating solid square cylinder and an outer isothermal circular boundary is performed. The two orientations considered for the inner solid square cylinder are the square-on-side (SOS) and the square-on-edge (SOE). A cylindrical annulus with an inner solid circular cylinder (CC) of equivalent heat generation is also studied for the purpose of comparison. The flow equations cast in vorticity-stream function form and the energy equations are solved using numerical methods. The steady state results show that the flow in the annulus is characterized by double or quadruple vortex patterns. Of the dimensionless maximum solid temperature, average solid temperature and average inner boundary temperature, the first two are much sensitive to solid-to-fluid thermal conductivity ratio. The dependence of the average Nusselt number on the average inner boundary temperature based Grashof number is found to be in good agreement with the heat transfer data computed for differentially heated annuli with isothermal boundaries, within the parametric space covered. Correlations as functions of Grashof number are developed for the estimation of various quantities of interest for different configurations, aspect ratios and thermal conductivity ratios. The results are expected to be useful in the design of thermal systems such as the spent nuclear fuel casks and underground transmission cables.

© 2008 Elsevier Inc. All rights reserved.

1. Introduction

Natural convection heat transfer is an inexpensive, reliable and noise-free method of heat removal and has been a subject of intensive research due to its technological applications ranging from nuclear reactors, thermal storage systems, cooling of electronic components, aircraft fuselage insulation to underground electrical transmission cables. In particular, natural convection in horizontal annuli has received considerable attention in the literature because of the fundamental nature of the geometry. Isothermal wall boundary conditions have been much studied compared to isoflux conditions.

Natural convection heat transfer in the gap between the horizontal concentric isothermal cylinders has been first investigated experimentally by Beckmann (1931) with air, hydrogen, carbon dioxide as the test fluids in order to obtain the overall heat transfer coefficient. An important contribution in the measurement of the temperature field in the gap between two horizontal isothermal cylinders filled with air has been made by Grigull and Hauf (1966) using a Mach-Zehnder interferometer. Kuehn and Goldstein

(1976a,b, 1978, 1980) have performed further investigations on natural convection in horizontal annulus experimentally and numerically to determine the influence of Rayleigh number, Prandtl number, diameter ratio and eccentricity. Farouk and Güçeri (1982) have presented numerical solutions for the steady-state, two-dimensional laminar and turbulent natural convection between two horizontal isothermal concentric cylinders. Chang et al. (1983) have analysed the natural convection heat transfer in an enclosure formed by concentric isothermal square inner and circular outer cylinders, using the Galerkin finite element method. Boyd (1983) has theoretically studied the natural convection heat transfer across an annulus with a circular outer boundary and an irregular inner boundary. Boyd (1984) has also reported an experimental study using Mach-Zehnder interferometer, with a hexagonal inner cylinder, oriented such that two of the six surfaces are horizontal. Tsui and Tremblay (1984) have numerically solved the transient natural convection heat transfer problem between two horizontal isothermal cylinders, applicable to underground electrical transmission line. Transient natural convection in this geometry was also studied numerically and experimentally by Castrejon and Spalding (1988). Shu et al. (2001) have numerically studied the natural convective heat transfer in a horizontal eccentric annulus between an isothermal square outer and a heated isothermal circular inner cylinder using differential quadrature (DQ) method.

* Corresponding author. Tel.: +91 80 22932971; fax: +91 80 23600648.
  E-mail address: mecgsvln@mecheng.iisc.ernet.in (G.S.V.L. Narasimham).
[1] Present address: Vellore Institute of Technology, Vellore 632 014, India.

Nomenclature

a	thermal diffusivity ($m^2\,s^{-1}$)
A	aspect ratio [ratio of the side of inner square cylinder to the diameter of the outer cylinder, $S/(2R_o)$]
A_c	cross-sectional area of the inner solid cylinder, (m^2)
A_{ib}	surface area per unit axial length of the inner cylinder ($m^2\,m^{-1}$)
c	specific heat capacity, ($J\,kg^{-1}\,K^{-1}$)
g	acceleration due to gravity ($m\,s^{-2}$)
Gr	heat generation based Grashof number [$= (g\,\beta\,\Delta T R_o^3)/v_f^2$, $\Delta T = \dot{Q}_v R_o^2/\lambda_f$]
Gr_T	temperature based Grashof number [$= (g\,\beta\,\Delta T R_o^3)/v_f^2$, $\Delta T = T_{av,ib} - T_r$]
i, j	grid point indices
n	normal distance (m)
Nu	Nusselt number
P	perimeter (m)
Pr	Prandtl number
R_i	equivalent radius of the inner cylinder (m)
R_o	radius of the outer cylinder (m)
Ra	Rayleigh number ($= Gr \cdot Pr$)
$\dot{q}$	heat flux ($W\,m^{-2}$)
$\dot{Q}_v$	volumetric heat generation ($W\,m^{-3}$)
S	side of the inner square cylinder (m)
t	time (s)
T	temperature (K)
u, v	velocities in the x- and y-directions ($m\,s^{-1}$)
v_r, v_θ	velocities in the radial and tangential directions ($m\,s^{-1}$)

Greek symbols

α	heat transfer coefficient ($W\,m^{-2}\,K^{-1}$)
β	volumetric expansion coefficient (K^{-1})
η	dynamic viscosity (Pa s)
θ	angular coordinate (radians)
λ	thermal conductivity ($W\,m^{-1}\,K^{-1}$)
v	kinematic viscosity ($m^2\,s^{-1}$)
ξ	distance along cylinder surface (m)
ρ	density ($kg\,m^{-3}$)
ϕ_x, ϕ_y	angles between gravity vector and x- and y-axes, respectively (radians)
ψ	stream function ($m^2\,s^{-1}$)
ω	vorticity (s^{-1})

Subscripts

av	average
eq	equivalent
l	local
max	maximum
ib, ob	inner and outer boundaries, respectively
r	reference
s, f	solid and fluid, respectively

Superscript

*	dimensionless quantity

Few studies have considered isoflux inner wall boundary condition. Kumar (1988) and Kumar and Keyhani (1990) have studied the natural convection heat transfer in horizontal annuli with inner and outer cylinders maintained at constant heat flux and temperatures, respectively. Yoo (1998, 1999a,b) has made systematic investigations on the Prandtl number dependence of natural convective flows in horizontal annuli with a heated (isoflux) inner cylinder and an isothermally cooled outer cylinder. Transitions of natural convection in an annulus between horizontal isothermal cylinders have been theoretically investigated by Mizushima et al. (2001) by obtaining bifurcation diagrams of steady solutions. Dual free convective flows in a horizontal annulus formed by an inner cylinder maintained at constant heat flux and the outer cylinder isothermally cooled have been numerically investigated by Yoo (2003) for fluids of Prandtl number in the range 0.2–1.

Rotem (1972) has studied the conjugate free convection in a horizontal annulus using a series expansion technique. The inner cylinder core carries either a line source along its axis or a distributed heat source or both and the outer cylinder is maintained at a constant temperature. Bubnovich and Kolesnikov (1986), Kolesnikov and Bubnovich (1988) and Lacroix and Joyeux (1996) have numerically studied the conjugate problem of natural convection in horizontal annuli to investigate the influence of the finite conductance of the cylinder walls.

Natural convection in annuli driven by an inner heat generating cylinder has received very less attention in the past. Such problems arise in applications like transportation and storage of spent nuclear fuel casks, underground transmission cables and in other thermal energy systems, where there's a continuous heat generation. For instance, spent nuclear fuel casks contain one or more canisters of circular, square or hexagonal cross-section, containing bundles of fuel rods arranged in triangular or square arrays. Our problem deals with modelling of one such canister as a heat generating solid with an equivalent thermal conductivity, as the natural convection

in the fill gas is often negligible. Methods of calculating equivalent thermal conductivity of such arrays of tubes or rods have been presented by Manteufel and Todreas (1994).

The objective of the present work is to numerically investigate the conjugate natural convection in a horizontal annulus formed by a heat generating inner cylinder of square cross-section and an isothermal circular outer cylinder and to find the temperature and the velocity distributions in the annulus as well as the temperature field in the square solid. The results presented are steady-state results obtained from time-dependent formulations by time marching. For comparison, the case of a heat generating solid circular cylinder of equal cross-sectional area is also computed. In addition, the natural convection in differentially heated annuli with isothermal boundaries is computed for all the configurations. From the results of the conjugate problem, the average inner boundary temperature is determined and the equivalent Grashof number based on the average inner boundary and outer boundary temperature difference is calculated. The variation of the average Nusselt number with this Grashof number is compared with the heat transfer data of differentially heated annuli and a good agreement is found between the two sets of results.

2. The physical model and the coordinate system

The physical model and the coordinate system for the present work are shown in Fig. 1a. A circular cylinder, ABCDA, of radius R_o, is located in the first quadrant in such a way that the coordinate axes are tangential to it with the positive direction of the x-axis towards right and the positive direction of the y-axis vertically upwards as shown. The quantities $\hat{i}$ and $\hat{j}$ are the unit vectors along the x- and y-directions. EFGHE is a solid square cylinder of side S, located concentrically inside the circular cylinder. For generality, the gravity vector $\vec{g}$ is shown to make angles ϕ_x and ϕ_y with the
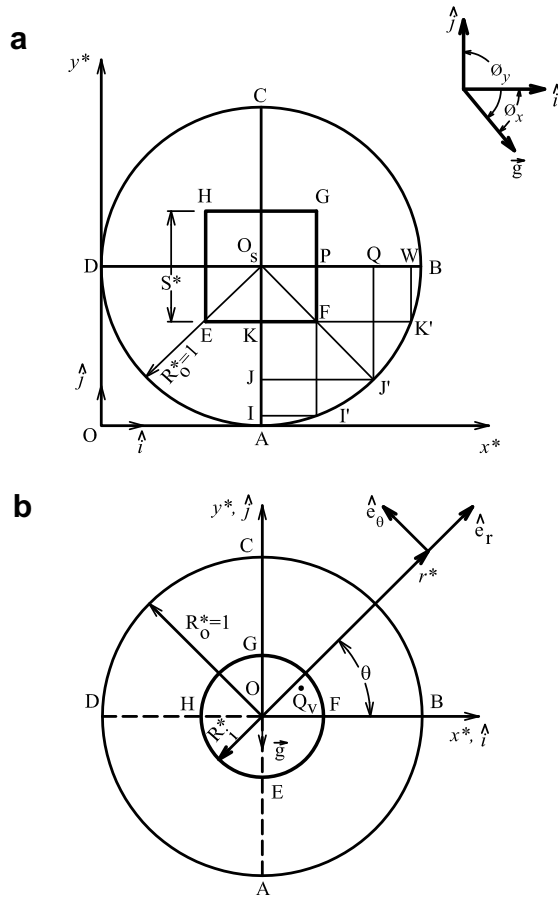
Fig. 1. The physical model and coordinate system for the annulus with (a) inner solid square cylinder and (b) inner solid circular cylinder.

x- and y-directions respectively. The annulus is assumed to be sufficiently long so that the flow and the temperature fields can be taken as invariant along the z-direction, neglecting the end effects. Two orientations of the inner cylinder are considered, namely, the SOS (Square-On-Side, $\phi_x = 90°$ and $\phi_y = 180°$) and the SOE (Square-On-Edge, $\phi_x = 45°$ and $\phi_y = 135°$). The cartesian coordinate system is chosen to describe the geometry for the SOS and SOE configurations.

At times less than or equal to zero, the fluid inside the annulus is quiescent with uniform temperature at T_r. For times greater than zero, the inner solid square begins to generate heat with a volumetric heat generation rate of $\dot{Q}_v$, which is transferred to the fluid, whereas the outer cylinder is isothermally cooled with the temperature maintained at $T_o = T_r$.

In order to compare the results of the conjugate natural convection in the horizontal annulus formed between a square inner and a circular outer cylinder, computations are also performed for the horizontal circular cylindrical annulus (denoted as CC), obtained by replacing the inner solid square cylinder with a heat generating solid circular cylinder of equivalent cross-sectional area, EFGHE of radius R_i as shown in Fig. 1b. This problem is described in cylindrical coordinates with the gravity vector acting vertically downwards and $\hat{e}_r$ and $\hat{e}_\theta$ denoting the unit vectors along r- and θ-directions, respectively. The azimuthal angle θ is measured from OB in the counter-clockwise direction. However, the governing equations are presented only in cartesian coordinates (for the SOS and SOE cases) for brevity. The governing equations in cylindrical coordinates are available, for example, in Kuehn and Goldstein (1976a). The solid energy equation can be obtained from

the fluid energy equation by choosing zero velocities and setting the properties to those of the solid.

3. Formulation

3.1. Governing equations

The flow and temperature distributions are assumed to be two-dimensional and are governed by continuity, Navier–Stokes, and fluid and solid energy equations. The radiative heat transfer, viscous dissipation and compressibility effects of air are considered to be negligible. The effect of density variation causing the buoyancy force is taken into account through the Oberbeck-Boussinésq approximation. Other thermophysical properties of the fluid and those of solid are assumed to be independent of temperature.

The vorticity transport, stream function and fluid and solid energy equations in dimensionless form for the SOS and SOE cases are:

$$\frac{\partial \omega^*}{\partial t^*} + \frac{\partial}{\partial x^*}(u^*\omega^*) + \frac{\partial}{\partial y^*}(v^*\omega^*)$$
$$= \left(\frac{\partial^2 \omega^*}{\partial x^{*2}} + \frac{\partial^2 \omega^*}{\partial y^{*2}}\right) + Gr\frac{\partial T_f^*}{\partial y^*}\cos\phi_x - Gr\frac{\partial T_f^*}{\partial x^*}\cos\phi_y, \quad (1)$$

$$\frac{\partial^2 \psi^*}{\partial x^{*2}} + \frac{\partial^2 \psi^*}{\partial y^{*2}} = -\omega^*, \quad (2)$$

$$\frac{\partial T_f^*}{\partial t^*} + \frac{\partial}{\partial x^*}(u^*T_f^*) + \frac{\partial}{\partial y^*}(v^*T_f^*) = \frac{1}{Pr}\left(\frac{\partial^2 T_f^*}{\partial x^{*2}} + \frac{\partial^2 T_f^*}{\partial y^{*2}}\right) \quad (3)$$

$$\rho_s^* c_s^* \frac{\partial T_s^*}{\partial t^*} = \frac{\lambda_s^*}{Pr}\left(\frac{\partial^2 T_s^*}{\partial x^{*2}} + \frac{\partial^2 T_s^*}{\partial y^{*2}}\right) + \frac{1}{Pr}, \quad (4)$$

where λ_s^* is the solid-to-fluid thermal conductivity ratio and

$$\omega^* = \frac{\partial v^*}{\partial x^*} - \frac{\partial u^*}{\partial y^*}; \quad u^* = \frac{\partial \psi^*}{\partial y^*}; \quad v^* = -\frac{\partial \psi^*}{\partial x^*}. \quad (5)$$

The system of non-dimensionalisation is

$$t^* = \frac{tv_f}{R_o^2}, \quad x^* = \frac{x}{R_o}, \quad y^* = \frac{y}{R_o}, \quad u^* = \frac{uR_o}{v_f}, \quad v^* = \frac{vR_o}{v_f},$$

$$\omega^* = \frac{\omega R_o^2}{v_f}, \quad \psi^* = \frac{\psi}{v_f}, \quad \rho_s^* = \frac{\rho_s}{\rho_f}, \quad c_s^* = \frac{c_s}{c_{p,f}}, \quad \lambda_s^* = \frac{\lambda_s}{\lambda_f}, \quad (6)$$

$$T^* = \frac{(T - T_r)}{\Delta T}, \quad \Delta T = \frac{\dot{Q}_v R_o^2}{\lambda_f}, \quad Gr = \frac{g\beta\Delta T R_o^3}{v_f^2}, \quad Pr = \frac{\eta_f c_{p,f}}{\lambda_f}.$$

3.2. Initial and boundary conditions

The initial conditions at $t^* = 0$ correspond to a quiescent state with uniform temperature. At $t^* > 0$, no-slip hydrodynamic condition exists on the inner and outer boundaries of the annulus. The thermal boundary conditions at the solid–fluid interface are the heat flux continuity and no temperature jump, which can be written as:

$$\lambda_s^* \frac{\partial T_s^*}{\partial n_s^*} = \frac{\partial T_f^*}{\partial n_f^*}, \quad T_s^* = T_f^*, \quad (7)$$

For the CC case, the condition at the center is that the temperature remains finite. In view of the symmetry of flow and temperature fields for the SOS, SOE and CC cases, the dimensionless stream function on both the surfaces of the annulus is taken as zero (for example, Rotem, 1972; Tsui and Tremblay, 1984; Chmaissem et al., 2002). The vorticity on the inner and outer boundaries is calculated using Eq. (5).

3.3. Nusselt numbers

The local Nusselt number $Nu_{l,ib}$ is given by:

$$Nu_{l,ib} \equiv \frac{\alpha_{l,ib}R_o}{\lambda_f} = -\frac{1}{T^*_{av,ib}}\left[\frac{\partial T^*_f}{\partial n^*_f}\right]_{l,ib} = \frac{\dot{q}^*_{l,ib}}{T^*_{av,ib}}. \qquad (8)$$

The average Nusselt number $Nu_{av,ib}$ on the inner boundary is given by:

$$\int_{ib}\alpha_{l,ib}\left(T_{av,ib}-T_r\right)d\xi_{ib} = \int_{ib}-\lambda_f\left[\frac{\partial T_f}{\partial n_f}\right]_{l,ib}d\xi_{ib} = \dot{Q}_v S^2, \qquad (9)$$

i.e.,
$$\int_{ib}Nu_{l,ib}\,T^*_{av,ib}\,d\xi^*_{ib} = \int_{ib}-\left[\frac{\partial T^*_f}{\partial n^*_f}\right]_{l,ib}d\xi^*_{ib} = S^{*2}, \qquad (10)$$

where ξ^*_{ib} is the dimensionless distance measured along the periphery of the inner boundary from the bottom-most point (i.e., midpoint of the bottom surface in SOS, bottom corner in SOE and lowest point in CC) in the counter-clockwise direction.

The above equation takes the form:

$$Nu_{av,ib} = \frac{1}{P^*_{ib}}\int_{ib}Nu_{l,ib}\,d\xi^*_{ib} = \frac{1}{P^*_{ib}}\int_{ib}-\frac{1}{T^*_{av,ib}}\left[\frac{\partial T^*_f}{\partial n^*_f}\right]_{l,ib}$$
$$d\xi^*_{ib} = \frac{S^{*2}}{T^*_{av,ib}P^*_{ib}}, \qquad (11)$$

where P^*_{ib} and $T^*_{av,ib}$ are the dimensionless perimeter and the dimensionless average temperature on the inner boundary.

Similarly, the average Nusselt number $Nu_{av,ob}$ on the outer boundary is given by:

$$Nu_{av,ob} = \frac{1}{P^*_{ob}}\int_{ob}Nu_{l,ob}\,d\xi^*_{ob} = \frac{1}{P^*_{ob}}\int_{ob}-\frac{1}{T^*_{av,ib}}\left[\frac{\partial T^*_f}{\partial n^*_f}\right]_{l,ob}$$
$$d\xi^*_{ob} = \frac{S^{*2}}{T^*_{av,ib}P^*_{ob}}, \qquad (12)$$

where ξ^*_{ob} is the dimensionless distance measured along the circumference of the outer boundary from the bottom-most point in the counter-clockwise direction. P^*_{ob} is the dimensionless perimeter of the outer boundary.

The relation between the average Nusselt numbers on the inner and the outer boundaries is obtained from the Eqs. (11) and (12):

$$P^*_{ib}Nu_{av,ib} = P^*_{ob}Nu_{av,ob} = \frac{S^{*2}}{T^*_{av,ib}}. \qquad (13)$$

The above definitions of Nusselt numbers also apply to the CC case for which $P^*_{ib} = 2\pi R^*_i$ and $\pi R^{*2}_i = S^{*2}$, where $R^*_i = R_i/R_o$.

4. Method of solution

4.1. Mesh generation

The two orientations of the inner square cylinder, SOS and SOE, yield configurations that are symmetric about the vertical line passing through the center of the square as can be seen from Fig. 1a. The symmetry lines for the SOS and SOE configurations are respectively AC and the line passing through the diagonal HF. Keeping this in view, the grid is generated in such a way that it can be used for both the configurations by suitably deploying the gravity vector.

For the SOS configuration, the gravity vector is along the direction O_sK. Considering the quarter circle AO_sB, the projections of the point F determine the points I′ and K′. The line O_sF, when extended, meets the curved boundary at J′. The projections of I′, J′ and K′ determine respectively I, P; J, Q and K, W. AI is divided into the required number of mesh spacings, say a, and the corresponding points are successively projected on to curved segment AI′ and

from there to O_sP. Similarly, IJ is divided into the required number of mesh spacings, say b, and the corresponding points are successively projected on to the curved segment I′J′ and from there to PQ. The distributions of points on O_sP and PQ are transferred onto the segments O_sK and KJ in the same order, which are in turn used to generate the points on QW and WB respectively. The nodes are generated as mirror images in the other quadrants.

When the spacings are uniform in the segments AI and IJ, a non-uniform spacing results in the segments O_sP and PQ because of the non-linear nature of the outer circle. In order to have a control on the distribution of grid points in either direction, the mesh in each of these segments is generated with the help of the one-dimensional, inverse hyperbolic function based transformation of Roberts (1971). Typical grids for the aspect ratios 0.2 and 0.4 are shown in Figs. 2a and b, respectively.

4.2. Discretisation

The steady-state results are obtained as the long-time solutions to time-dependent equations using finite difference techniques. A numerical formulation is developed by discretizing the governing equations. The convective terms are discretized by the donor-cell method (Torrance and Rockett, 1969; Vafai and Ettefagh, 1990). The diffusive terms are discretized with central differences using second-order accurate analogues. The boundary vorticity for the SOS and SOE cases is evaluated using definition of vorticity in terms of velocities. For the CC case, Thom's boundary vorticity conditioning is employed (Roache, 1998). The local fluid temperature gradients are evaluated with third-order accurate finite difference representations at the points on the inner boundary for all the configurations. For the outer boundary, second-order accurate expressions for the local temperature gradient in each direction are used to obtain the normal temperature gradient for the SOS and SOE configurations, while for the CC configuration, third-order accurate expressions are employed. The numerical quadrature is performed using the high-accuracy scheme of Gill and Miller (1972).

For the CC configuration, in order to resolve the center point singularity, the solid energy equation in cartesian form is discretized at the center of the inner solid circle with the first grid circle radius as the mesh spacing. Choosing the number of the angular spacings as a multiple of four, such discretized equations are written for all the required mutually perpendicular orientations of the radial lines and are summed up. The relation for the center temperature is obtained from the summed up discretized equations.

The heat flux continuity condition can be discretized directly using two-point one-sided differences. However, such a discretization, while neglecting the thermal capacitance of solid and fluid each half cell width, does not also account for the heat generation in half cell width region in the solid. In view of this, a four-cell method is devised for the numerical treatment of the interface temperature, which does not suffer from these drawbacks and which implicitly accounts for the heat flux continuity. The method of calculating the interface temperature is briefly presented in the Appendix. For the numerical treatment of the solid–fluid interface in the CC case, a two-cell method, the development of which is similar to the four-cell method, is employed.

4.3. Solution procedure

A segregated solution approach is adopted, which consists in solving the discretised equations of energy, vorticity and stream function equations in succession for each time step with a point Gauss-Seidel iterative method. Sufficient number of global iterations on the set of equations are performed over each time step for better coupling of velocity and temperature fields. The time
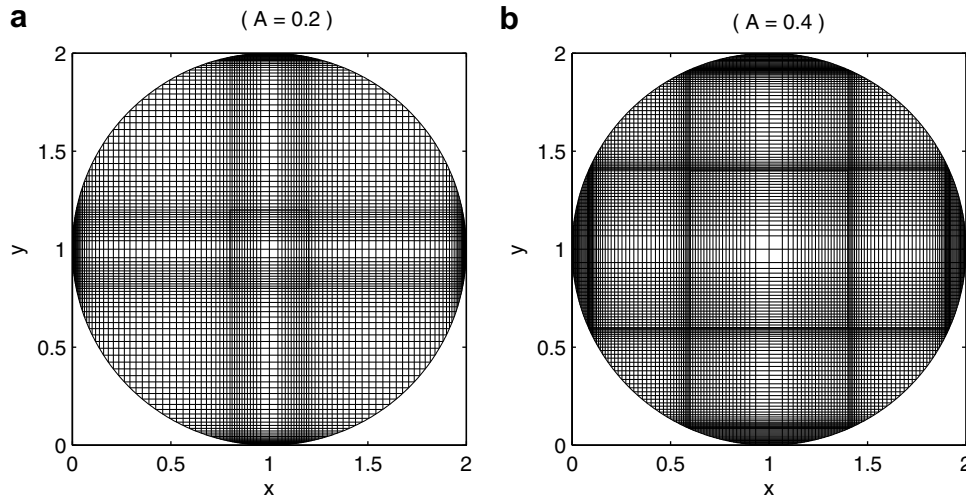
a (A = 0.2)

b (A = 0.4)

Fig. 2. Typical grid for the SOS/SOE configurations for (a) $A = 0.2$ (121×121) and (b) $A = 0.4$ (161×161).

step is chosen as a multiple (typically 50) of that obtained from the combined Courant-Friedrichs-Lewy and diffusion number restrictions as shown in Roache (1998) applicable to explicit methods. A relative convergence criterion of 5×10^{-5} on the maximum dimensionless temperature is chosen for the global iteration process at each time step. The criterion for the attainment of steady-state is that the relative difference of the maximum temperature in the domain over 50 time steps should be less than 10^{-6}. The energy balances on the inner and outer boundaries with respect to the total heat generation are used as additional checks for the attainment of steady-state. The heat transfer rates across the inner and outer boundaries are obtained by integration of the local fluid temperature gradient around the respective peripheries. To obtain faster convergence to steady-state, the quantity $\rho_s^* c_s^*$ is set equal to unity.

The results from the derived variable (vorticity-stream function) approach have been verified against those predicted by a pressure correction algorithm on a collocated mesh (Kim and VanOverbeke, 1991) and an excellent agreement has been found between the two approaches.

4.4. Calculation of energy balance

The heat generation $\dot{Q}_{gen}$ in the inner solid cylinder is S^{*2}. The heat transfer rate $\dot{Q}_{ib}$ across the inner cylinder is given by:

$$\dot{Q}_{ib} = \int_{ib} -\left[\frac{\partial T^*}{\partial n^*}\right]_{1,ib} d\xi^*_{ib}. \tag{14}$$

Similarly, the heat transfer rate across the outer boundary can be written as:

$$\dot{Q}_{ob} = \int_{ob} -\left[\frac{\partial T^*}{\partial n^*}\right]_{1,ob} d\xi^*_{ob}. \tag{15}$$

The derivative $\partial T^*/\partial n^*$ in the above expression is evaluated as the scalar product of $\vec{\nabla} T^*$ and the unit normal vector $\hat{n}^*$ directed towards the outer boundary, where $\vec{\nabla}$ is the dimensionless gradient operator in cartesian coordinates. The unit normal vector is $(x^* - x^*_c)\hat{i} + (y^* - y^*_c)\hat{j}$, where (x^*, y^*) is any point on the outer boundary and (x^*_c, y^*_c) are the coordinates of the center of the inner solid cylinder. The relative energy balances EB_{ib} and EB_{ob} on the inner and the outer boundaries are determined by the expressions $|\dot{Q}_{gen} - \dot{Q}_{ib}|/\dot{Q}_{gen}$ and $|\dot{Q}_{gen} - \dot{Q}_{ob}|/\dot{Q}_{gen}$, respectively. The energy balance for the CC case is calculated in a similar manner.

4.5. Code validation

A computer program is developed and run on the ALPHA work stations at the Supercomputer Education and Research Center, Indian Institute of Science, Bangalore, India. All the calculations are performed with the double-precision arithmetic, for which the word length is 32 bits.

To ensure the correctness of the program for the SOS and SOE configurations, the code is validated with the results reported by Chang et al. (1983). Table 1 presents a comparison of the present results for the overall equivalent thermal conductivity λ^*_{eq} (defined as the ratio of the average Nusselt number on the inner boundary to that for an equivalent pure-conduction case), with those of Chang et al. (1983). The results for the pure conduction case are obtained by setting the Rayleigh number to zero. The present equivalent thermal conductivity values agree well with the results of Chang et al. (1983) in most cases.

The computer program for the circular cylindrical annulus, CC has been validated with the results of Kuehn and Goldstein

Table 1
Comparison of the present solutions with the results of Chang et al. (1983)

Orientation	A	Ra	λ^*_{eq} Present solutions	λ^*_{eq} Chang et al. (1983)	% Deviation
SOS	0.2	1.0×10^3	1.035	1.003	3.2
		5.0×10^3	1.393	1.346	3.5
		1.0×10^4	1.712	1.644	4.1
		5.0×10^4	2.676	2.457	8.9
		1.0×10^5	3.157	2.846	10.9
SOE	0.2	1.0×10^3	1.045	1.004	4.1
		5.0×10^3	1.411	1.346	4.8
		1.0×10^4	1.743	1.647	5.8
		5.0×10^4	2.727	2.482	9.8
		1.0×10^5	3.247	2.900	11.9
SOS	0.4	1.0×10^3	1.007	1.002	0.5
		5.0×10^3	1.064	1.043	2.0
		1.0×10^4	1.159	1.126	2.9
		5.0×10^4	1.934	1.617	19.6
		1.0×10^5	2.344	1.991	17.7
SOE	0.4	1.0×10^3	1.007	1.002	0.5
		5.0×10^3	1.072	1.046	2.4
		1.0×10^4	1.187	1.153	2.9
		5.0×10^4	1.818	1.762	3.1
		1.0×10^5	2.226	2.142	3.9

Table 2
Comparison of the present solutions for cylindrical annulus (CC) with the results of Kuehn and Goldstein (1976a)

Ra	Location	λ_{eq}^* Present solutions	λ_{eq}^* Kuehn and Goldstein (1976a)	% Deviation
10^2	Inner	1.002	1.000	0.20
	Outer	1.002	1.002	0.00
10^3	Inner	1.088	1.081	0.67
	Outer	1.088	1.084	0.39
3×10^3	Inner	1.396	1.404	0.57
	Outer	1.395	1.402	0.50
6×10^3	Inner	1.712	1.736	1.38
	Outer	1.712	1.735	1.32
10^4	Inner	1.977	2.010	1.64
	Outer	1.976	2.005	1.45
2×10^4	Inner	2.375	2.405	1.25
	Outer	2.372	2.394	0.92
3×10^4	Inner	2.628	2.661	1.24
	Outer	2.624	2.643	0.72
5×10^4	Inner	2.971	3.024	1.75
	Outer	2.965	2.973	0.27
7×10^4	Inner	3.218	3.308	2.72
	Outer	3.208	3.226	0.56

(1976a) reported for the horizontal annulus formed between isothermally cooled outer and heated inner cylinders. The comparison of the present results with those of Kuehn and Goldstein (1976a) is given in Table 2. The results agree well with each other, the largest difference being 2.72%.

4.6. Grid sensitivity tests

In order to select the mesh that gives reasonably accurate solutions, grid sensitivity tests are conducted with five different meshes on the conjugate problem with the number of grid points on each diameter varying from 61 to 141 for the aspect ratio 0.2 and 65 to 193 for the aspect ratio 0.4. The other parameters are $\lambda_s^* = 10$ and $Gr = 10^8$. Based on these tests a 121×121 mesh and a 161×161 mesh are selected for the aspect ratios 0.2 and 0.4, respectively, for both SOS and SOE configurations. For the CC case, equal number of mesh spacings are employed in the radial and angular directions and the number of mesh spacings are varied from 60 to 100 and an 81×80 mesh is finally chosen. This grid contains respectively 33 and 41 grid points in the solid region for equivalent aspect ratios of 0.2 and 0.4.

5. Results and discussion

Results are obtained for the heat generation and outer radius based Grashof number (Gr) ranging from 10^4 to 10^9, for solid-to-fluid thermal conductivity ratios (λ_s^*) of 1, 10 and 100, and for the aspect ratios (A) of 0.2 and 0.4, with air as the working medium ($Pr = 0.708$) for the SOS, SOE and CC configurations. As can be seen from the results, the heat generation based Grashof number Gr is generally two to three orders of magnitude higher than the temperature difference based Grashof number Gr_T. In view of this, laminar steady-state flow solutions could be obtained for Gr values as high as 10^9. Since the computations cover a wide parametric space, selected results are presented.

5.1. Isotherms and streamlines

The isotherm and streamline maps are presented in the Figs. 3–5 for the SOS, SOE and CC configurations respectively for $\lambda_s^* = 10$,

the Grashof number ranging from 10^5 to 10^8 for both the aspect ratios.

For the SOS configuration, for $A = 0.2$ and at $Gr = 10^5$, the isotherms are nearly concentric indicating a pseudo-conductive regime as called by Grigull and Hauf (1966). The corresponding streamlines are kidney-shaped and are symmetric about the vertical diameter. At $Gr = 10^6$, the isotherms in the vicinity of the solid square become inverted egg-shaped and the contours are closely placed at the bottom corners of the square as compared to those at the top corners. The center of the corresponding kidney-shaped streamlines now shifts slightly above the horizontal line passing through the top face of the square. At $Gr = 10^7$, the isotherms are distorted and a plume is found to develop from the top face of the inner square cylinder. Thermal boundary layers are also observed at the inner and the outer surfaces and are characterized by the densely distributed isotherms. The strength of the circulation increases and the center of rotation of the streamlines (which is a stagnation point) moves further and lies above the horizontal line passing through the top face. The buoyant plume above the inner cylinder impinges upon the outer cylinder at the top, creating the thinnest boundary layer. This warm fluid then moves in a boundary layer adjacent to the outer cylinder towards the bottom. Careful examination of the isotherms reveals that a temperature inversion exists in part of the region between the two boundary layers with the fluid near the cold outer surface being warmer than that closer to the hot inner surface. The inner streamlines of the core are stretched with the center further drifting upwards. The fluid at the bottom of the annulus appears to be almost stagnant.

At $Gr = 10^8$, the single plume is separated into two, each of which is found to emanate from the corner of the top face. The mechanism for this transition may be explained as follows. In the SOS configuration, the top face of the square cylinder is a heated surface facing upwards. At lower Grashof numbers, the top surface tends to produce a circulation with the fluid rising upwards from the middle portion. The fluid rising from the vertical faces is entrained into the plume formed above the top surface, giving rise to a double-eddy (one on each side of the vertical centreline) circulation in the annulus. Beyond $Gr = 10^8$, the side flow is not entrained into the plume above the top surface but tends to rise upwards from the side faces, due to the higher velocities. This upward flow prevents the fluid from rising above the middle portion of the top surface and produces a shear-driven circulation in an opposite sense, i.e., with fluid descending towards the middle portion and flowing out from the end portions of the top face. For instance, in the right half of the annulus, the upper eddy has counter-clockwise circulation and the lower one has clockwise circulation, with an inclined plume formed near the top right corner of the solid. Thus in the annulus, there occurs a double plume, since there is a symmetrically placed inclined plume in the other vertical half. The isotherms in the solid become denser compared to those in the fluid region. Two small cells are formed above the top face whose circulation is in the direction opposite to that of the bigger cells on the corresponding side, while the centers of the larger cells move towards the outer surface. The increase in the values of the maximum and the minimum stream function is less pronounced because of the formation of the bicellular pattern on each side. The stagnant region at the bottom of the annulus is found to increase. For all the Grashof numbers, a refraction is observed in the isotherms at the solid–fluid interface which is in accordance with the heat flux continuity condition. For $A = 0.4$, the onset of the double plume occurs at a lower Grashof number 10^7 with the appearance of a dual flow in the annulus.

For the SOE and CC configurations, for both the aspect ratios, the isotherms and streamlines are symmetric about the vertical center line. Quadruple vortex cores are observed for Grashof numbers 10^5 and 10^6 in case of SOE configuration and the bifurcation from qua-
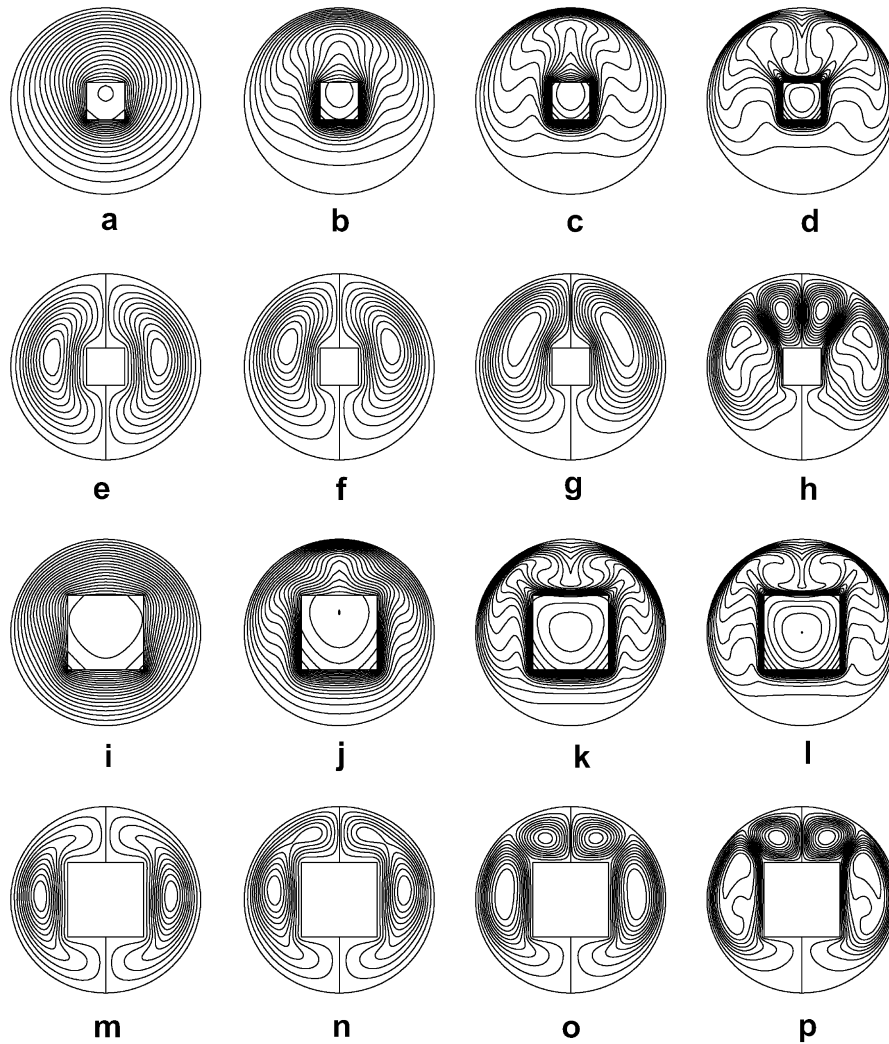
Fig. 3. Isotherm and streamline maps for the SOS configuration for $\lambda_s^* = 10$. Grashof number: a,e,i,m $\rightarrow 10^5$, b,f,j,n $\rightarrow 10^6$, c,g,k,o $\rightarrow 10^7$ and d,h,l,p $\rightarrow 10^8$. $A = 0.2$ for a–h and $A = 0.4$ for i–p. Isotherms: (a) (0.0, 0.034 [0.0017]), (b) (0.0, 0.022 [0.0011]), (c) (0.0, 0.014 [0.0007]), (d) (0.0, 0.009 [0.00045]), (i) (0.0, 0.079 [0.00395]), (j) (0.0, 0.055 [0.00275]), (k) (0.0, 0.033 [0.00165]) and (l) (0.0, 0.022 [0.0011]). Streamlines: (e) (−3.09, 3.09 [0.309]), (f) (−11.33, 11.33 [1.133]), (g) (−25.14, 25.14 [2.514]), (h) (−37.43, 37.43 [3.743]), (m) (−3.37, 3.37 [0.337]), (n) (−14.09, 14.09 [1.409]), (o) (−27.14, 27.14 [2.174]) and (p) (−50.83, 50.83 [5.083]).

druple vortex cores to the double vortex pattern is found to occur at $Gr = 8.1 \times 10^6$. No double plume is found in SOE and CC configurations.

5.2. Variation of local Nusselt number

The variation of local Nusselt number along the inner and the outer boundaries for the SOS and SOE cases for $A = 0.4$ and a wide range of Grashof number is shown in Fig. 6 for $\lambda_s^* = 1$ and 10.

For $\lambda_s^* = 1$, as shown in Figs. 6a–h, the minimum value of the Nusselt number occurs at all the corners for the SOS case, whereas for the SOE, the minimum is found at the right and the left corners. While the maximum values occur at the mid-points of all the faces for the SOE configuration, the mid-points of the right and the left faces register the maximum values of Nusselt number for the SOS case. On the outer cylinder, while the minimum values always occur at the bottom-most point, the maximum occurs at the top-most point for both the SOS and SOE cases. An exception is observed at the Grashof number 10^8 for the SOS configuration with the maximum occurring at the points where the double plume impinges on to the outer boundary. A slight dip is found at the peak of the curve for the SOE case for which the maximum Nusselt number

on the outer boundary is found to occur just adjacent to the the top-most point. This could be due to the adverse effect of the sharp-edged corner on the convection heat transfer as reported by Chang et al. (1983). In view of the fact that the faces of the square are parallel to the coordinate lines, there occurs a discontinuity in the local Nusselt number at each corner, where two local Nusselt numbers can be computed in each direction.

While an increasing and decreasing trend occurs for each face of the square for $\lambda_s^* = 1$, an opposite trend is observed on the inner boundary for the case of $\lambda_s^* = 10$ as shown in Figs. 6i–p with an enhanced Nusselt number at the corners. This could be due to the fact that at the higher λ_s^*, the generated heat is diverted largely to the corners owing to the decreased natural convective film resistance at the corners.

Figs. 7a and b show the variations of the local Nusselt number for the CC case for $A = 0.4$ and $\lambda_s^* = 10$ at the Grashof number 10^7 for the inner and the outer boundary, respectively. It is found that the variation is smooth along the inner as well as the outer boundary due to the absence of the sharp corners. The minimum value on the inner boundary and the maximum value on the outer boundary lie at the top-most points on the corresponding surfaces while the maximum value on the inner boundary and the minimum value on
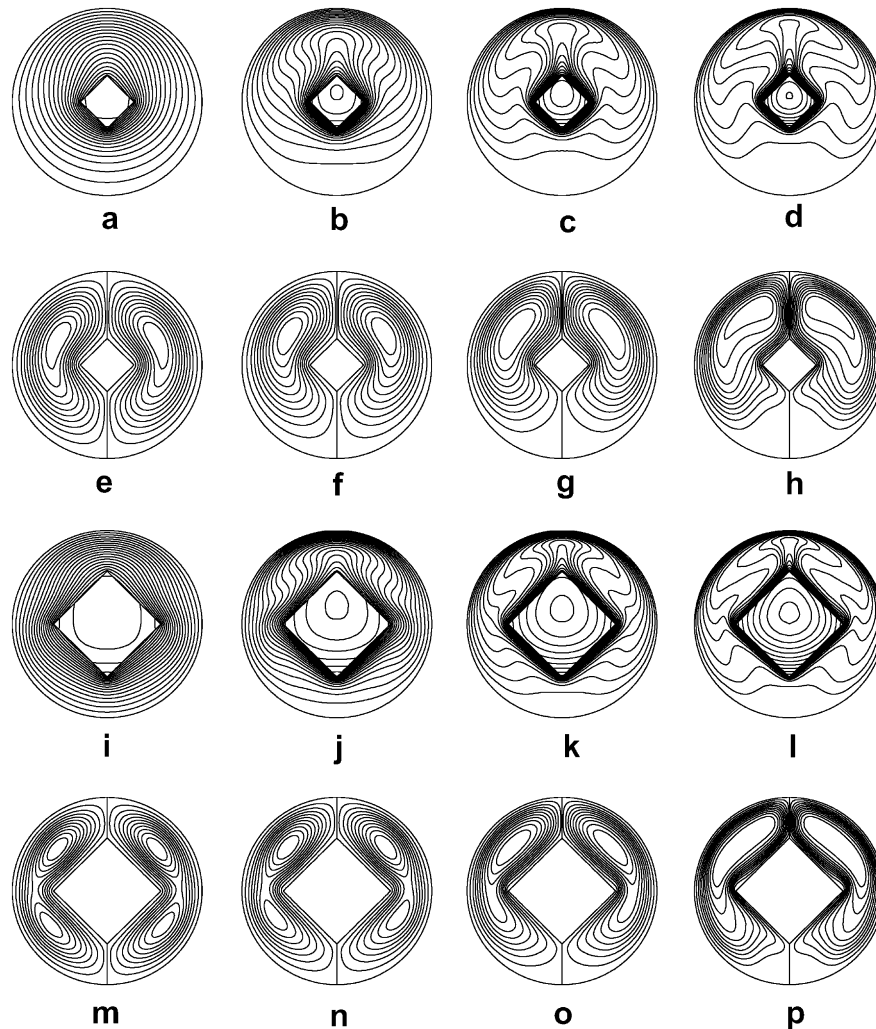
Fig. 4. Isotherm and streamline maps for the SOE configuration for $\lambda_s^* = 10$. Grashof number: a,e,i,m $\rightarrow 10^5$, b,f,j,n $\rightarrow 10^6$, c,g,k,o $\rightarrow 10^7$ and d,h,l,p $\rightarrow 10^8$. $A = 0.2$ for a–h and $A = 0.4$ for i–p. Isotherms: (a) (0.0, 0.034 [0.0017]), (b) (0.0, 0.021 [0.00115]), (c) (0.0, 0.014 [0.0007]), (d) (0.0, 0.009 [0.00045]), (i) (0.0, 0.078 [0.0039]), (j) (0.0, 0.052 [0.0026]), (k) (0.0, 0.033 [0.00165]), and (l) (0.0, 0.022 [0.0011]). Streamlines: (e) (−2.85, 2.85 [0.285]), (f) (−11.08, 11.08 [1.108]), (g) (−25.82, 25.82 [2.582]), (h) (−44.94, 44.94 [4.494]), (m) (−2.94, 2.94 [0.294]), (n) (−13.78, 13.78 [1.378]), (o) (−34.45, 34.45 [3.445]) and (p) (−57.17, 57.17 [5.717]).

the outer boundary lie at the bottom-most point on the respective surfaces. The same trend is observed for other λ_s^* and Grashof numbers.

5.3. Dimensionless temperature profiles

The variation of $T_{l,ib}^*$ for the SOS and SOE configurations is presented in Fig. 8a for $Gr = 10^8$, $\lambda_s^* = 10$ and $A = 0.4$. The figure shows that the variation of the local temperature is characterized by several local maxima with local minima occurring at the corners for the SOS and SOE configurations. Bell-shaped curves are observed for the CC case showing that the temperature is maximum at the top-most point and minimum at the bottom-most point of the inner boundary as seen in Fig. 8b. As the Grashof number increases, $T_{l,ib}^*$ decrease, other parameters remaining the same. Higher λ_s^* lead to the evening out of the temperature variation, although the trends remain the same for other Grashof numbers and aspect ratios.

5.4. Variation of various quantities with Grashof number

The variation of different quantities such as T_{max}^*, $T_{av,ib}^*$, $T_{av,s}^*$ and $Nu_{av,ib}$ with Grashof number are presented in Fig. 9 for λ_s^* of 1 (solid line), 10 (dashed line) and 100 (dotted line). For convenience, the data points for the SOS, SOE and CC configurations are indicated with square, diamond and circle symbols, respectively.

Figs. 9a and e refer to the variation of T_{max}^* with Grashof number for the aspect ratios 0.2 and 0.4, respectively. It is found that the maximum temperature always occurs inside the solid region. The T_{max}^* drops as the Grashof number increases for all λ_s^*. However, the drop is more rapid in the range of Grashof number $10^5–10^6$. In general, the SOE and the CC configurations yield the lowest and the highest T_{max}^*, the SOS lying between them, sometimes shifting towards that of SOE or that of CC. This shift, at higher Grashof numbers can be attributed to the development of the double plume, which enhances the heat transfer. It can be observed that the change in T_{max}^* is larger for the λ_s^* range 1–10 than for the range 10–100. In addition, the change in T_{max}^* between different configurations is more pronounced at higher λ_s^* for $A = 0.4$.

Fig. 9b and f show the variation of the $T_{av,s}^*$ with Grashof number. The behavior is the same as that of T_{max}^* inside the solid. The values for the CC case are generally higher than those for the SOS and the SOE configurations.

The variation of $T_{av,ib}^*$ with Grashof number is presented in Fig. 9c and g. For $A = 0.2$, there is no significant difference between the values for the different configurations and λ_s^*, as can be seen
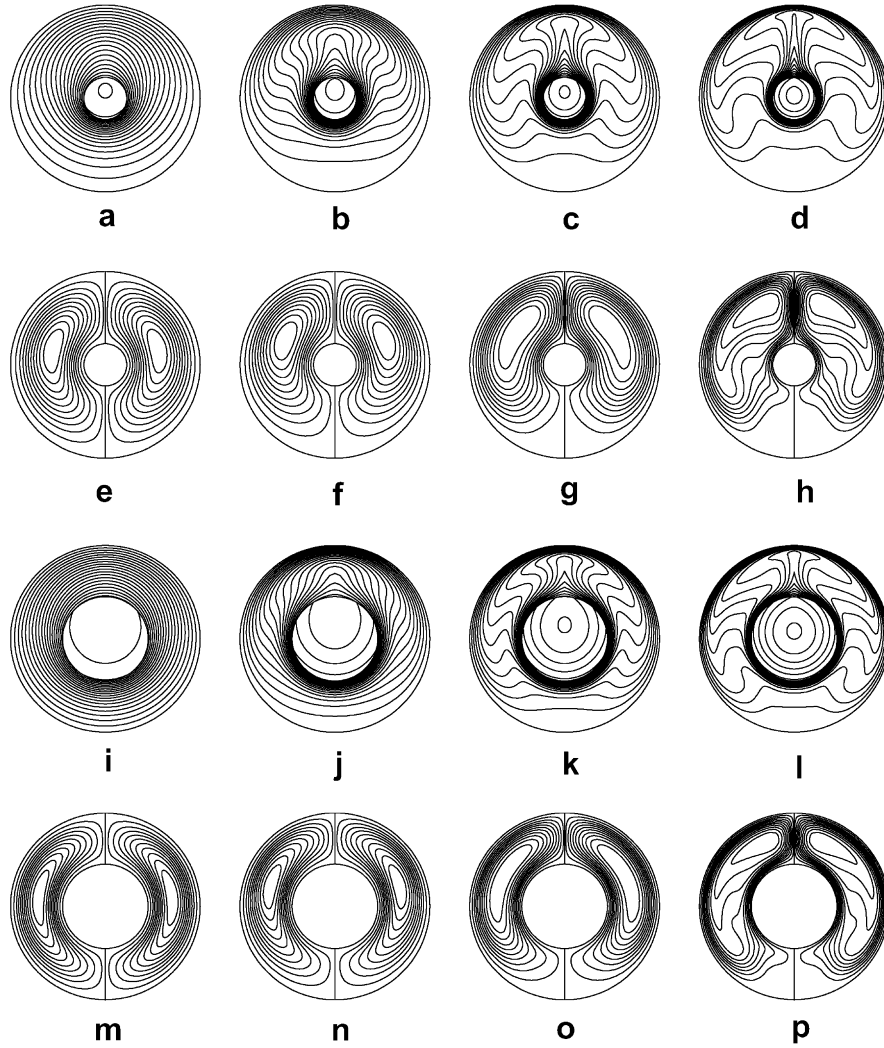
Fig. 5. Isotherm and streamline maps for the CC configuration for $\lambda_s^* = 10$. Grashof number: a,e,i,m $\rightarrow 10^5$, b,f,j,n $\rightarrow 10^6$, c,g,k,o $\rightarrow 10^7$ and d,h,l,p $\rightarrow 10^8$. $A = 0.2$ for a–h and $A = 0.4$ for i–p. Isotherms: (a) (0.0, 0.034 [0.0017]), (b) (0.0, 0.021 [0.00105]), (c) (0.0, 0.014 [0.0007]), (d) (0.0, 0.010 [0.0005]), (i) (0.0, 0.082 [0.0041]), (j) (0.0, 0.055 [0.00275]), (k) (0.0, 0.035 [0.00175]) and (l) (0.0, 0.024 [0.0012]). Streamlines: (e) (−3.16, 3.16 [0.316]), (f) (−11.84, 11.84 [1.184]), (g) (−25.55, 25.55 [2.555]), (h) (−47.01, 47.01 [4.071]), (m) (−3.02, 3.02 [0.302]), (n) (−13.89, 13.89 [1.389]), (o) (−32.07, 32.07 [3.207]) and (p) (−58.17, 58.17 [5.817]).

from the very closely spaced curves. For $A = 0.4$, the variation of $T_{av,ib}^*$ with Grashof number shows some dispersion for the different configurations and λ_s^*, but even this amounts to a maximum of about 15% at $Gr = 10^6$. It can be seen that slightly higher values of $T_{av,ib}^*$ occur for the higher λ_s^* for each of the configurations. The SOE configuration yields the lowest $T_{av,ib}^*$ compared to other configurations, although this difference is not very significant even for the case of $A = 0.4$.

Recalling that $Nu_{av,ib}$ is based on $T_{av,ib}^*$ and that for a given Gr, fluid, aspect ratio and R_o, the heat generation and hence the heat transfer is fixed, it can be concluded that the heat transfer coefficient $\alpha_{av,ib}$, and hence $Nu_{av,ib}$ will be rather insensitive to λ_s^* in view of the weak dependence of $T_{av,ib}^*$ on λ_s^*. Indeed, variation of $Nu_{av,ib}$ with Grashof number presented in Fig. 9d and h, shows that it is a weak function of λ_s^*. It is interesting to compare and contrast this behavior with that of $Nu_{l,ib}$ which shows significant variation with λ_s^*, as can be seen from the graphs presented earlier. The average Nusselt number increases with the Grashof number and the slope of the curve is small in the Grashof number range of 10^4–10^5 where a pseudo-conductive regime occurs. At $A = 0.2$, all the configurations register lower Nusselt numbers with an increase in λ_s^* at both lower and higher Grashof numbers. At $A = 0.4$, the same trend is observed for the SOE and the CC configurations while an opposite behavior is found for the SOS case at higher Grashof numbers. This could be attributed to the development of the double plume, the effect of which is predominant at higher λ_s^*.

The weak dependence of the $Nu_{av,ib}$ on the λ_s^* indicates that the thermal resistance offered by the convecting fluid in the annular region is generally small, while in the solid, an adjustment between the temperature gradient and thermal conductivity occurs while transferring a given amount of heat.

5.5. Average Nusselt number based on temperature-based Grashof number

In addition to the above results, a temperature difference based Grashof number Gr_T is determined for each set of the parameters and the Nusselt number is plotted against Gr_T. From the energy balance on the inner cylinder, the total heat generated by the cylinder is equal to the heat convected from the same, i.e., $\dot{Q}_v A_c = \alpha_{av,ib}(T_{av,ib} - T_{ob})A_{ib}$. Hence Gr_T is given by:

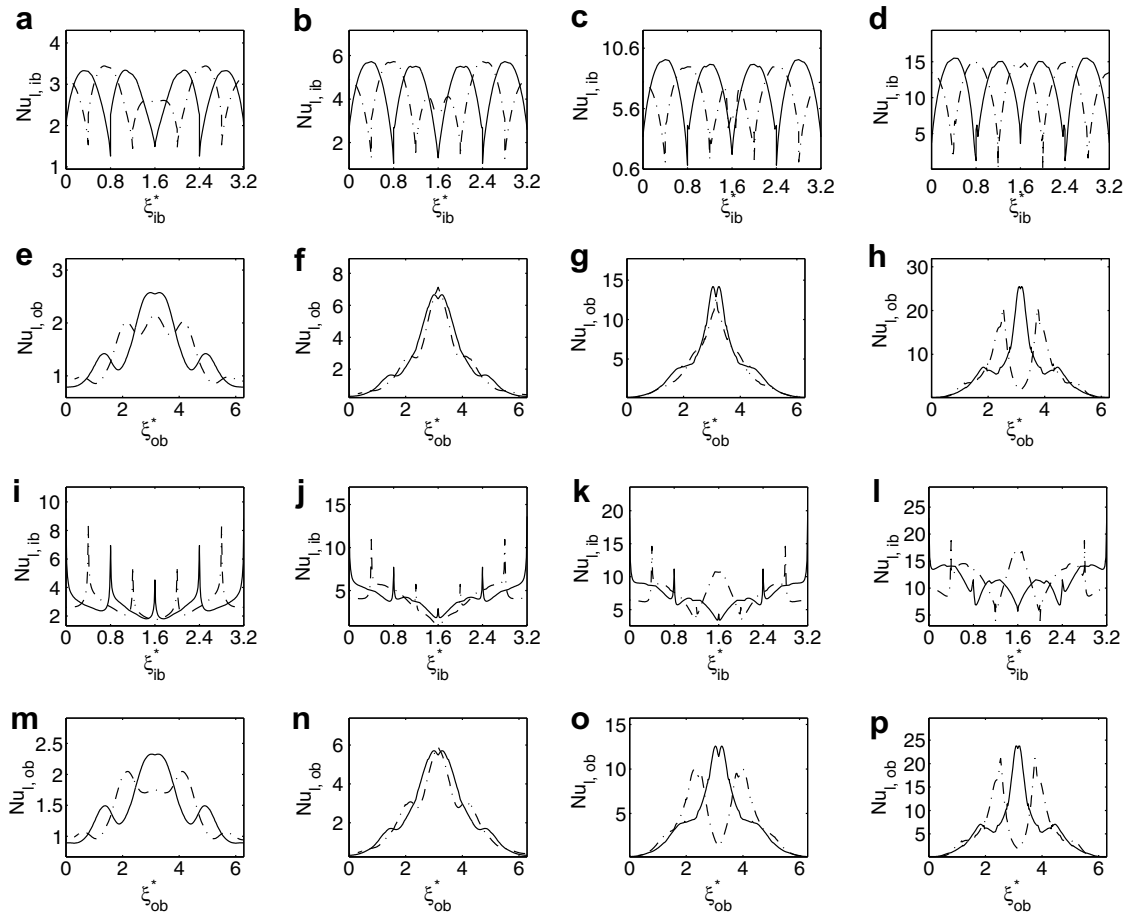$$Gr_T = \frac{Gr}{Nu_{av,ib}} \frac{A_c}{A_{ib} R_o}. \tag{16}$$

Fig. 6. Variation of local Nusselt number for the SOS (dot-dash line) and SOE (Continuous line) configurations for $A = 0.4$. Inner boundary: (a)–(d), outer boundary: (e)–(h), for $\lambda_s^* = 1$. Inner boundary: (i)–(l), outer boundary: (m)–(p), for $\lambda_s^* = 10$. $Gr = 10^5$, 10^6, 10^7, 10^8 for the figures in first to fourth columns respectively.
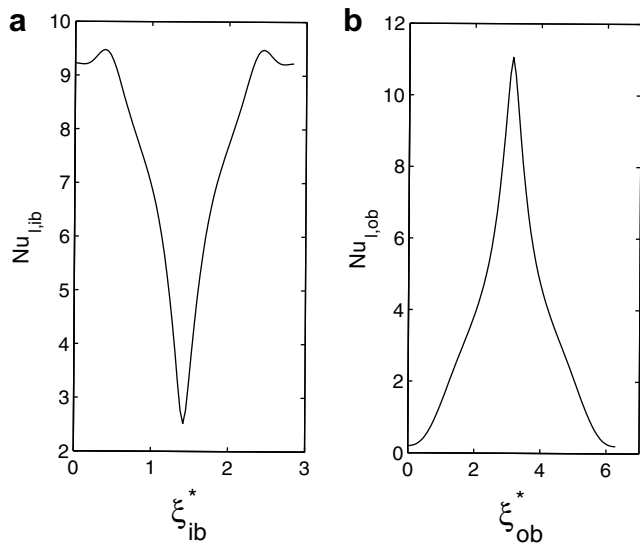

Fig. 7. Variation of local Nusselt number for the CC configuration for $A = 0.4$ and for $\lambda_s^* = 10$. (a) Inner boundary. (b) Outer boundary.
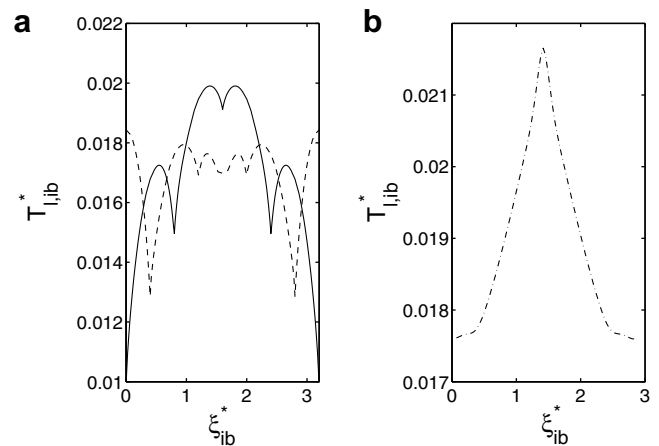

Fig. 8. Variation of dimensionless local temperature along the inner boundary for $\lambda_s^* = 10$, $A = 0.4$ and $Gr = 10^8$. (a) For SOS (dashed line) and SOE (solid line) configurations. (b) For CC configuration.

The factor $A_c/(A_{ib}R_o)$ equals $S^*/4$ and $R^*_i/2$ for the square and circular inner cylinders, respectively. In general, Gr_T is found to be less than Gr by two orders of magnitude. For instance, Table 3 gives the values of Gr and Gr_T for $\lambda_s^* = 10$ for the SOS and CC configurations.

Fig. 10 shows the variation of $Nu_{av,ib}$ with Gr_T for various configurations and for the different aspect ratios considered. This figure also includes the results for isothermal condition on the inner boundary.

In general, the various curves for a given aspect ratio are close to one another and here too, the differences due to the change in λ_s^* are small. However, from a closer examination, it can be stated that the curves for higher λ_s^* of 10 and 100 approach the isothermal
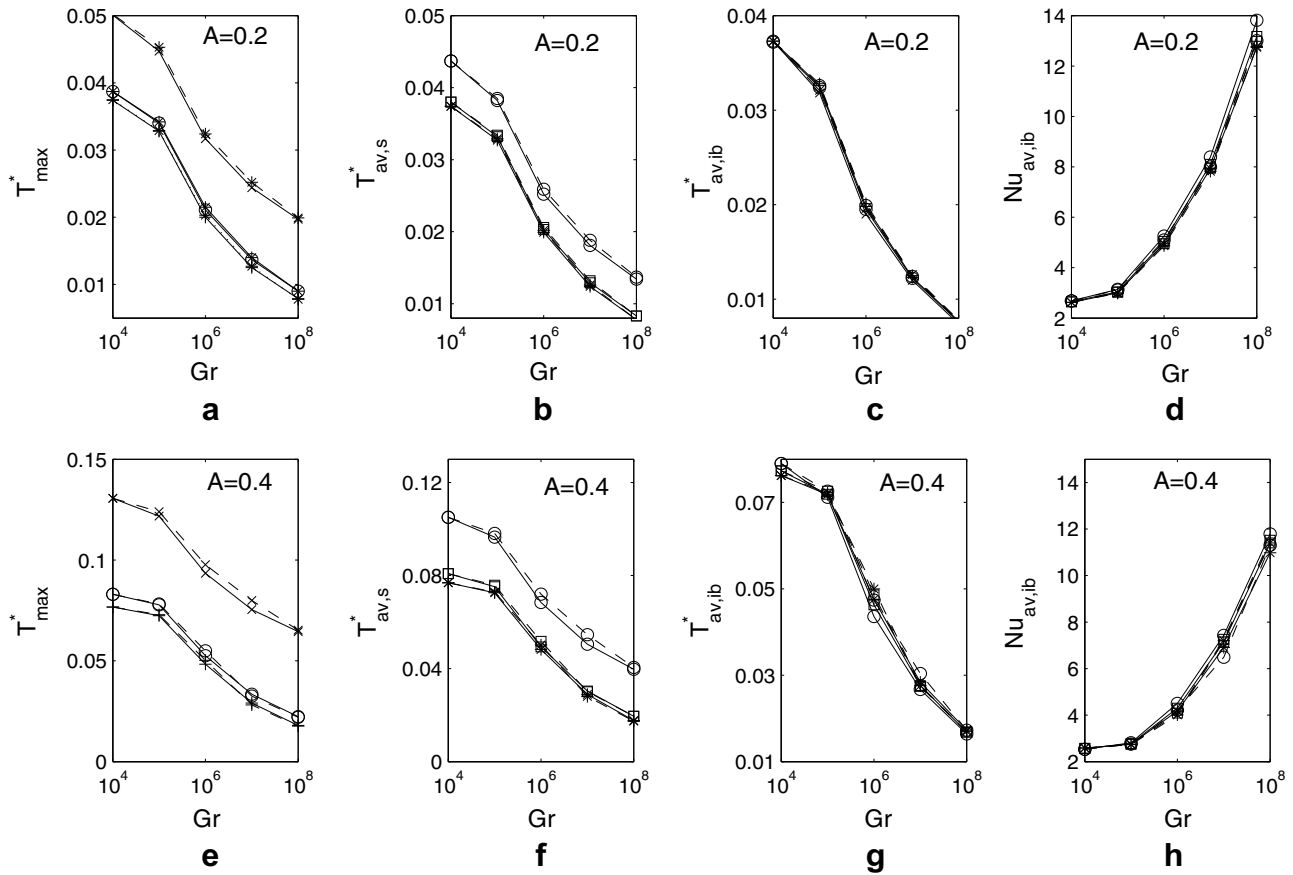
Fig. 9. Variation of T^*_{max}, $T^*_{av,s}$, $T^*_{av,ib}$ and $Nu_{av,ib}$ with Gr for λ^*_s: 1 (solid line), 10 (dashed line) and 100 (dotted line) and $A = 0.2$ (a, b, c and d) and for $A = 0.4$ (e, f, g and h), respectively. (The data points for the SOS, SOE and CC configurations are indicated with square, diamond and circle symbols, respectively.)

Table 3
Relation between heat generation based Grashof number Gr and the average inner boundary temperature based Grashof number Gr_T for $\lambda^*_s = 10$

Configuration	A	$Nu_{av,ib}$	Gr	Gr_T
SOS	0.2	7.94	10^7	1.25×10^5
		12.98	10^8	7.71×10^5
		22.98	10^9	4.35×10^6
SOS	0.4	7.26	10^7	2.75×10^5
		11.52	10^8	1.73×10^6
		21.67	10^9	9.23×10^6
CC	0.2	8.86	10^7	1.27×10^5
		13.50	10^8	8.36×10^5
		21.96	10^9	5.14×10^6
CC	0.4	7.61	10^7	2.96×10^5
		11.94	10^8	1.89×10^6
		19.28	10^9	1.17×10^7

case more closely for the CC and SOE configurations than for the SOS configuration.

In the experimental investigations of natural convection in annuli with differentially heated isothermal cylinders, the hotter inner cylinder is generally heated by a condensing vapor (with the colder outer cylinder cooled by water or liquid circulation). The present work shows that, within the scope of the parametric studies carried out, if electrical heating is used for the solid inner cylinder with the average surface temperature of the heat generating cylinder taken as the temperature for defining the temperature based Grashof number, reasonably accurate results for the average Nusselt number in terms of Gr_T and other parameters can be achieved,

even if the thermal conductivity of the inner solid cylinder is not large and even if a truly isothermal condition along the periphery of the inner cylinder does not exist.

On the other hand, if the interest lies in the prediction of maximum and average temperatures of the inner solid cylinder, as, for example, in spent nuclear fuel casks involving a known amount of heat generation, proper experimental investigation with due consideration to the temperature distribution in the solid or the solution of the conjugate natural convection problems is indeed necessary and important, particularly when λ^*_s are not very high.

5.6. Correlations from computed data

The heat transfer data obtained is correlated in terms of the parameters of the problem. The correlations for T^*_{max} are given in the Table 4.

It can be seen that at $A = 0.2$, there is not much difference between the coefficients and exponents for the correlations of different configurations for the corresponding thermal conductivity ratios, while the difference is larger for $A = 0.4$. This means that the geometry and orientation of the inner cylinder, i.e., square resting on side or edge or a circle, is important only at higher aspect ratios. In other words, at lower aspect ratios, the outer cylinder does not distinguish the exact geometry of the inner cylinder.

In view of the rather weak dependence of $Nu_{av,ib}$ on a particular configuration and λ^*_s, the following separate correlations, applicable to each aspect ratio are obtained. In constructing each of such correlations, the data pertaining to all the thermal conductivity ratios and configurations is included. With $Nu_{av,ib}$ determined, $Nu_{av,ob}$ can be easily found using Eq. (12).
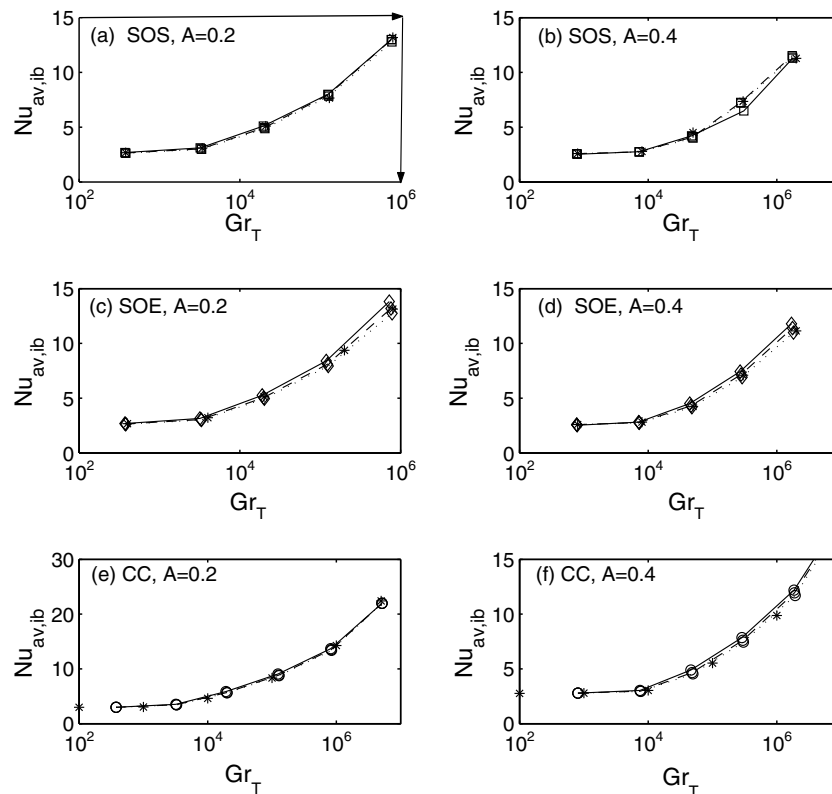
Fig. 10. Variation of $Nu_{av,ib}$ with dimensionless average temperature based Grashof number for various configurations. $A = 0.2$ for a,c,e and $A = 0.4$ for b,d,f. λ_s^*: 1 (continuous line), 10 (dashed line), 100 (dotted line), Isothermal inner boundary (asterisk).

Table 4
Correlations for the dimensionless maximum temperature

Configuration	A	λ_s^*	T_{max}^*	e_{ms}	C_c
SOS	0.2	1	$0.1337\,Gr^{-0.1017}$	0.0032	0.9835
		10	$0.2173\,Gr^{-0.1717}$	0.0110	0.9802
		100	$0.2215\,Gr^{-0.1777}$	0.0161	0.9626
SOS	0.4	1	$0.2881\,Gr^{-0.0794}$	0.0031	0.9634
		10	$0.4001\,Gr^{-0.1535}$	0.0229	0.9305
		100	$0.4408\,Gr^{-0.1693}$	0.0325	0.9195
SOE	0.2	1	$0.1342\,Gr^{-0.1030}$	0.0032	0.9841
		10	$0.2178\,Gr^{-0.1726}$	0.0103	0.9817
		100	$0.2180\,Gr^{-0.1769}$	0.0149	0.9650
SOE	0.4	1	$0.2913\,Gr^{-0.0821}$	0.0028	0.9697
		10	$0.3852\,Gr^{-0.1509}$	0.0178	0.9435
		100	$0.4192\,Gr^{-0.1655}$	0.0261	0.9318
CC	0.2	1	$0.1239\,Gr^{-0.0952}$	0.0036	0.9789
		10	$0.1952\,Gr^{-0.1625}$	0.0076	0.9846
		100	$0.2198\,Gr^{-0.1761}$	0.0104	0.9822
CC	0.4	1	$0.2619\,Gr^{-0.0707}$	0.0031	0.9670
		10	$0.4036\,Gr^{-0.1511}$	0.0133	0.9694
		100	$0.4816\,Gr^{-0.1720}$	0.0200	0.9646

$$Nu_{av,ib} = 0.4153\,Gr^{0.1883}\,(A = 0.2, e_{ms} = 0.0130, C_c = 0.9761), \quad (17)$$

$$Nu_{av,ib} = 0.4336\,Gr^{0.1758}\,(A = 0.4, e_{ms} = 0.0178, C_c = 0.9576). \quad (18)$$

In the above equations, e_{ms} denotes the mean square error and C_c, the correlation coefficient ($C_c = 1 - e_{ms}/\sigma^2$, where σ^2 is the variance).

6. Conclusions

Two-dimensional conjugate natural convection in horizontal cylindrical annuli formed between an inner heat generating solid square or circular cylinder and an outer isothermal circular cylinder is studied numerically. Computations are also performed for differentially heated annuli with isothermal boundaries and the heat transfer data is found to compare favorably with that of the conjugate problem expressed in terms of the average inner boundary temperature based Grashof number.

The results show that an additional circulation driven by the top horizontal face of the inner solid occurs on each side of the annulus for the SOS configuration at higher Grashof numbers for both the aspect ratios. For the SOE configuration, quadruple vortex cores exist in the annulus up to a Grashof number of 10^6 for aspect ratio 0.4. For other parameter ranges the flow exhibits double vortex cores in the annulus. The flow in the annulus is always bicellular for CC configuration. A thermal plume develops above the heated solid in all the configurations, whereas a double plume emerges from the upper corners in SOS configuration. A refraction of isotherms occurs at the solid–fluid interface and the degree of refraction is found to be higher for higher thermal conductivity ratios.

The $Nu_{l,ib}$ to a larger extent and the $T_{l,ib}^*$ to a smaller extent, are found to be sensitive to the solid-to-fluid thermal conductivity ratio, while, interestingly, $Nu_{av,ib}$ and $T_{av,ib}^*$ exhibit only a weak dependence on the thermal conductivity ratio. The λ_s^* has a negligible effect on the velocity fields. The behavior of various configurations is almost the same for λ_s^* of 10 and 100 indicating that the effect of thermal conductivity is more prominent in the range 1–10. With an inner heat generating cylinder, heat transfer data with a Grashof number based on ($T_{av,ib} - T_o$) would be reasonably accurate for isothermal differentially heated annuli, even though the thermal conductivity of the heat generating cylinder is not large. On the other hand, the maximum temperature does depend upon the solid thermal conductivity and hence requires the solution of the conjugate problem.
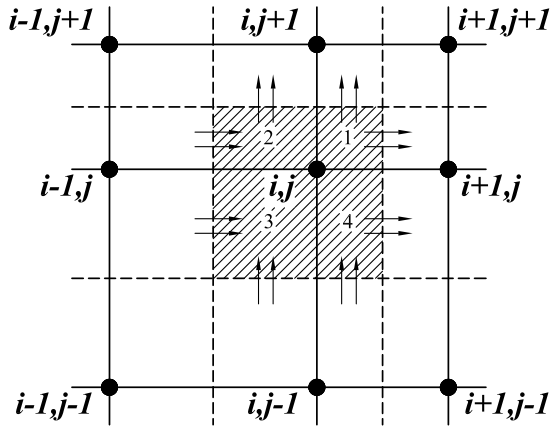
Fig. 11. Nine-point molecule for four-cell method of interface treatment.

Appendix. Numerical treatment of the solid–fluid interface for SOS and SOE configurations

As mentioned earlier, a four-cell method is employed for the SOS and SOE configurations for the calculation of the interface temperature. Fig. 11 shows a nine-point computational molecule with the central node (i,j) lying on the interface. The hatched regions are the four cells filled with either the solid or the fluid depending on the position of the boundary point. The heat generation is set to zero for the cell(s) filled with fluid. In view of the conduction heat flux or combined conduction and convection flux continuity across the internal boundaries separating the cells, only the conduction and convective flux contributions through the outer surfaces of each cell are considered. The net heat transfer is assumed to result in the internal energy rise of the composite cell, which is the ensemble of the four cells.

The energy equation in dimensionless form for any cell is:

$$\rho_k^* c_{p,k}^* \frac{\partial T_k^*}{\partial t^*} + \rho_k^* c_{p,k}^* \frac{\partial (u_k^* T_k^*)}{\partial x^*} + \rho_k^* c_{p,k}^* \frac{\partial (v_k^* T_k^*)}{\partial y^*}$$
$$= \frac{\lambda_k^*}{Pr} \left(\frac{\partial^2 T_k^*}{\partial x^{*2}} + \frac{\partial^2 T_k^*}{\partial y^{*2}} \right) + \frac{f_k}{Pr} \tag{A.1}$$

where k is the cell number and f_k is either zero or unity depending upon the cell.

The above equation is multiplied by $(\Delta t^* \Delta V_k^*)/\Delta c^*$, where $\Delta c^* = \Sigma \rho_k^* c_{p,k}^* \Delta V_k^*$ is the total heat capacity of the composite cell. Considering the discretized equations at the mid-point $(i+1/4, j+1/4)$ of the cell 1 and at the mid-point $(i-1/2, j+1/2)$ of the cell 2, the condition of flux continuity applied at the inner interface of cells 1 and 2 would cancel out the $-\lambda_k^*(\partial T_k^*/\partial x^*)$ terms. Similar reasoning applies to cells 2–3, 3–4 and 4–1. The discretized forms of the individual cells are summed up in order to obtain the governing equation for the composite cell, which is used for the determination of the interface temperature. This equation involves only the conduction and convection contributions shown by arrows in Fig. 11. The temperature of the composite cell is taken as the average temperature of the individual cells weighted with respect to the thermal capacitances, i.e.,

$$T_{i,j}^* = \frac{\sum_{k=1}^4 \rho_k^* c_{p,k}^* \Delta v_k^* T_k^*}{\sum_{k=1}^4 \rho_k^* c_{p,k}^* \Delta v_k^*} \tag{A.2}$$

References

Beckmann, W., 1931. Die wärmeübertragung in zylindrischen gasschichten bei natürlicher konvektion. Forsch. Geb. d. Ingenieurwesens 2 (5), 165–178.

Boyd, R.D., 1983. A correlation theory for steady natural convective heat transport in horizontal annuli. Trans. ASME J. Heat Transfer 105, 144–150.

Boyd, R.D., 1984. Interferometric study of natural convection heat transfer in a horizontal annulus with irregular boundaries. Nucl. Eng. Des. 83, 105–112.

Bubnovich, V.I., Kolesnikov, P.M., 1986. Conjugate transient heat transfer in laminar natural convection in a horizontal cylindrical annulus. J. Eng. Phys. 19, 1175–1181.

Castrejon, A., Spalding, D.B., 1988. An experimental and theoretical study of transient free-convection flow between horizontal concentric cylinders. Int. J. Heat Mass Transfer 31 (2), 273–284.

Chang, K.S., Won, Y.H., Cho, C.H., 1983. Patterns of natural convection around a square cylinder placed concentrically in a horizontal circular cylinder. Trans. ASME J. Heat Transfer 105, 273–280.

Chmaissem, W., Suh, S.J., Daguenet, M., 2002. Numerical study of the Boussinesq model of natural convection in an annular space: having a horizontal axis bounded by circular and elliptical isothermal cylinders. Appl. Ther. Eng. 22, 1013–1025.

Farouk, B., Güçeri, S.I., 1982. Laminar and turbulent natural convection in the annulus between horizontal concentric cylinders. Trans. ASME J. Heat Transfer 104, 631–636.

Gill, P.E., Miller, G.F., 1972. An algorithm for the integration of the unequally spaced points. Comput. J. 15, 80–83.

Grigull, U., Hauf, W., 1966. Natural convection in horizontal cylindrical annuli. Proc. 3rd Int. Heat Transfer Conf. 2, 154–158.

Kim, S.-W., VanOverbeke, T., 1991. On the anomaly of velocity–pressure decoupling in collocated mesh solutions. Nucl. Eng. Des., 103769.

Kolesnikov, P.M., Bubnovich, V.I., 1988. Non-stationary conjugate free-convective heat transfer in horizontal cylindrical coaxial channels. Int. J. Heat Mass Transfer 31 (6), 1149–1156.

Kuehn, T.H., Goldstein, R.J., 1976a. An experimental and theoretical study of natural convection in the annulus between horizontal concentric cylinders. J. Fluid Mech. 100 (4), 695–719.

Kuehn, T.H., Goldstein, R.J., 1976b. Correlating equations for natural convection heat transfer between horizontal circular cylinders. Int. J. Heat Mass Transfer 19, 1127–1134.

Kuehn, T.H., Goldstein, R.J., 1978. An experimental study of natural convection heat transfer in concentric and eccentric horizontal cylindrical annuli. Trans. ASME J. Heat Transfer 100, 638–640.

Kuehn, T.H., Goldstein, R.J., 1980. A parametric study of Prandtl number and diameter ratio effects on natural convection heat transfer in horizontal cylindrical annuli. Trans. ASME J. Heat Transfer 102, 768–770.

Kumar, R., 1988. Study of natural convection in horizontal annuli. Int. J. Heat Mass Transfer 31 (6), 1137–1148.

Kumar, R., Keyhani, M., 1990. Flow visualization studies of natural convective flow in a horizontal cylindrical annulus. Trans. ASME J. Heat Transfer 112, 784–787.

Lacroix, M., Joyeux, A., 1996. Coupling of wall conduction with natural convection from heated cylinders in a rectangular enclosure. Int. Commun. Heat Mass Transfer 23 (1), 143–151.

Manteufel, R.D., Todreas, N.E., 1994. Analytic formulae for the effective conductivity of a square or hexagonal array of parallel tubes. Int. J. Heat Mass Transfer 31 (4), 647–657.

Mizushima, J., Hayashi, S., Adachi, T., 2001. Transitions of natural convection in a horizontal annulus. Int. J. Heat Mass Transfer 44, 1249–1257.

Roache, P.J., 1998. Fundamentals of Computational Fluid Dynamics. Hermosa Publishers, Albuquerque, New Mexico.

Roberts, G.O., 1971. Computational meshes for boundary layer problems. In: Holt, M. (Ed.), Proceedings of the Second International Conference on Numerical Methods in Fluid Dynamics. Springer-Verlag, Berlin, pp. 171–177.

Rotem, Z., 1972. Conjugate free convection from horizontal conducting cylinders. Int. J. Heat Mass Transfer 15, 1679–1693.

Shu, C., Xue, H., Zhu, Y.D., 2001. Numerical study of natural convection in an eccentric annulus between square outer cylinder and a circular inner cylinder using a DQ method. Int. J. Heat Mass Transfer 44, 3321–3333.

Torrance, K.E., Rockett, J.A., 1969. Numerical study of natural convection in an enclosure with localized heating from belowcreeping flow to the onset of laminar instability. J. Fluid Mech. 36, 33–54.

Tsui, Y.T., Tremblay, B., 1984. On transient natural convection heat transfer in the annulus between concentric horizontal cylinders with isothermal surfaces. Int. J. Heat Mass Transfer 27 (1), 103–111.

Vafai, K., Ettefagh, J., 1990. Thermal and fluid flow instabilities in buoyancy-driven flows in open-ended cavities. Int. J. Heat Mass Transfer 33 (10), 2329–2344.

Yoo, J.-S., 1998. Natural convection in a narrow horizontal cylindrical annulus. Int. J. Heat Mass Transfer 41, 3055–3073.

Yoo, J.-S., 1999a. Prandtl number effect on bifurcation and dual solutions in natural convection in a horizontal annulus. Int. J. Heat Mass Transfer 42, 3279–3290.

Yoo, J.-S., 1999b. Prandtl number effect on transition of free-convective flows in a wide-gap horizontal annulus, Int. Commun. Heat Mass Transfer 26 (6), 811–817.

Yoo, J.-S., 2003. Dual free-convective flows in a horizontal annulus with a constant heat flux wall. Int. J. Heat Mass Transfer 46, 2499–2503.